Identification and Manipulation of Defects in Black Phosphorus

Rishav Harsh, Sourav Mondal, Devina Sharma, Mehdi Bouatou, Cyril Chacon, Maxim Ilyn, Celia Rogero, Vincent Repain, Amandine Bellec, Yann Girard, et al.

Identification and Manipulation of Defects in Black Phosphorus

Rishav Harsh,[†,‡,△] Sourav Mondal,[¶,§,△] Devina Sharma,[¶,△] Mehdi Bouatou,[†] Cyril Chacon,[†] Maxim Ilyn,[‖] Celia Rogero,[‖,⊥] Vincent Repain,[†] Amandine Bellec,[†] Yann Girard,[†] Sylvie Rousset,[†] Raman Sankar,[#] Woei Wu Pai,[@] Shobhana Narasimhan,[¶] and Jérôme Lagoute[*,†]

†*Université de Paris, CNRS, Laboratoire Matériaux et Phénomènes Quantiques, 75013, Paris, France.*

‡*Present address: Donostia International Physics Center DIPC, Donostia-San Sebastian, Basque Country 20018, Spain*

¶*Theoretical Sciences Unit and School of Advanced Materials, Jawaharlal Nehru Centre for Advanced Scientific Research, Jakkur, Bangalore 560064, India*

§*Present address: School of Physics, Trinity College Dublin, Dublin-2, Ireland*

‖*Centro de Física de Materiales (CFM-MPC) Centro Mixto CSIC-UPV/EHU, E-20018 Donostia-San Sebastian, Spain*

⊥*Donostia International Physics Center DIPC, Donostia-San Sebastian, Basque Country 20018, Spain*

#*Institute of Physics, Academia Sinica, Taipei 11529, Taiwan, ROC*

@*Center for Condensed Matter Sciences, National Taiwan University, Taipei 106 Taiwan, Republic of China*

△*Contributed equally to this work*

E-mail: jerome.lagoute@u-paris.fr

Abstract

We identify and manipulate commonly occurring defects in black phosphorus, combining scanning tunneling microscopy experiments with density functional theory calculations. A ubiquitous defect, imaged at negative bias as a bright dumbbell extending over several nanometers, is shown to arise from a substitutional Sn impurity in the second sublayer. Another frequently observed defect type is identified as arising from an interstitial Sn atom; this defect can be switched to a more stable configuration consisting of a Sn substitutional defect + P adatom, by application of an electrical pulse via the STM tip. DFT calculations show that this pulse-induced structural transition switches the system from a non-magnetic configuration to a magnetic one. We introduce States Projected Onto Individual Layers (SPOIL) quantities which provide information about atom-wise and orbital-wise contributions to bias-dependent features observed in STM images.

TOC Graphic

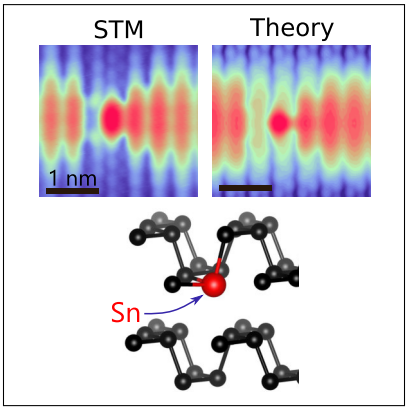

Black phosphorus (BP) consists of two-dimensional layers of phosphorus atoms (phosphorene) bonded by van der Waals interactions.[1] Unlike graphene,[2] BP has the advantage that it is a semiconductor whose band gap varies from ~ 0.3 eV in bulk BP, to up to 2.0 eV for a single layer.[3–5] Due to the puckered atomic structure of phosphorene layers, BP shows significant in-plane anisotropy in electronic, optoelectronic and thermal properties.[5–8]

Identifying the nature of native defects in BP and controlling their properties by external excitation are among current challenges for the exploitation of BP as a functional material. While defects in BP can be a limiting factor for materials performance, they can also confer desired properties.[9] Defects on the BP surface have been imaged using scanning tunneling microscopy (STM).[10–16] A commonly observed defect feature is an asymmetric dumbbell shape, extending several nanometers along the armchair direction; this has also been associated as the source of p-doping found in BP crystals. However, there is hitherto no consensus in the literature on the type of defect corresponding to such a dumbbell feature: some authors have identified the dumbbells as arising from monovacancies (MVs),[11,13,17] whereas others have concluded they arise from neutral or charged Sn substitutional defects.[12,16] Further confusion has arisen from scanning tunneling spectroscopy (STS) data on these defects from different groups showing peaks at different energies.[11,12,16]

Identification of the nature of the defects imaged in STM requires input from theoretical calculations on several possible defect structures. Until now, it has proved difficult to perform full-fledged density functional theory (DFT) calculations on candidate defect systems because of the extended length scales over which the effect of the defects are manifested. Therefore, previous authors have made use of tight binding calculations,[11,16] and/or modeled the defect as a hydrogenic acceptor[12,16] whose ground and first excited states look like an ellipse and dumbbell, respectively. We note that to date, no studies have shown a successful match between theoretically simulated and experimental STM images; indeed, previous authors reported that their simulated STM images of a MV or an Sn impurity in the topmost phosphorene sublayer (Sn-1) resulted in localized features quite different from the extended

dumbbell imaged experimentally.[12] We note too that the identification of the dumbbells as arising from MVs is called into question by MVs having a very low diffusion barrier, and also being unstable with respect to divacancies.[16] We therefore believe that there are still several open questions regarding the nature of experimentally observed defects in BP.

In this study, we have combined low temperature STM experiments (at 4.6 K) and DFT calculations to identify the nature of point defects in a BP sample. We have calculated STM images for a large set of defect configurations. To obtain an unambiguous identification, we then correlate experimental and simulated STM images at both negative and positive bias, as well as experimental STS results and theoretically obtained results for the projected density of states (PDOS). We find an excellent match for the ubiquitous dumbbell defects with a Sn substitutional defect in the lower plane of the topmost phosphorene layer. We have also observed another type of defect, not reported earlier, that can be switched experimentally to a more stable configuration. DFT calculations indicate that this also corresponds to a switch from a non-magnetic to a magnetic configuration.

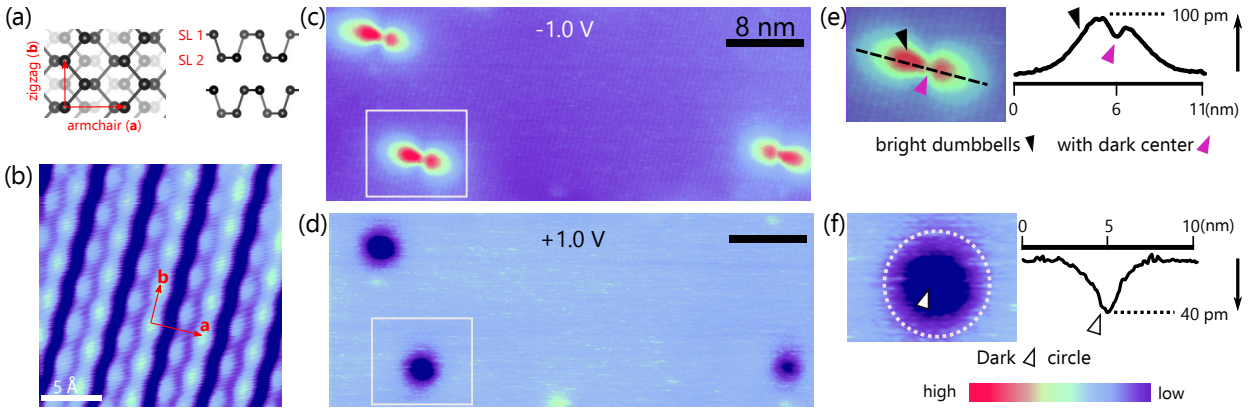

Figure 1: **Black phosphorus: defects at positive and negative bias.** (a) Schematic of BP crystal structure: top view (left) and side view (right). Red arrows indicate in-plane lattice vectors **a** and **b**. SL 1 and SL 2 denote sublayers of P atoms within the topmost phosphorene layer. (b) High resolution STM image of black phosphorus surface (sample bias voltage $V = -500$ mV, current setpoint $I_t = 20$ pA). Larger area STM topography images showing (c) dumbbell-shaped features at negative (-1.0 V) bias and (d) circular features at positive bias (1.0 V). Enlarged view of dumbbell defect along with linescan profile at (e) negative and (f) positive bias. Some salient features of the image are indicated by colored triangular markers: bright dumbbell shape at negative bias (black); dark center between two lobes at negative bias (magenta); dark dot with dark center at positive bias (white).

Side and top views of the atomistic structure of BP are shown in Fig. 1(a). Each phosphorene monolayer is comprised of an upper and a lower sublayer (SL1 and SL2 respectively in side view in right panel). Fig. 1(b) is an atomic resolution STM image of a defect-free region of a BP surface, obtained by cleaving under ultrahigh vacuum conditions [see Supporting Information (SI)]. In Fig. 1(b), zigzag rows of P atoms (light blue dots) along the [010] direction can be clearly seen. In Figs. 1(c) and 1(d) we show STM images of native defects. At negative bias, these defects have an asymmetric dumbbell shape oriented along the armchair direction and extending over ~ 8 nm. Such features have been remarked on by previous authors.[11,12,16,17] Importantly, we observe that on going from negative to positive bias, there is a contrast reversal [see Figs. 1(e) and 1(f)] and shape change, so that these same defects (labeled as type-**A** defects) now appear as dark circles; this has not been noted previously in the literature. We identify five salient features of defect-**A**: **(1)** bright contrast (higher LDOS with respect to pristine BP) at negative bias, **(2)** dumbbell shape at negative bias, **(3)** comparatively dark center (see magenta marker) between the lobes of the dumbbell at negative bias, **(4)** dark contrast (lower LDOS) with respect to pristine BP at positive bias, and **(5)** circular shape at positive bias.

Another type of defect that we frequently observe appears as a bright circular dot at both negative and positive bias (labeled as type-**B** defect). Several examples of **A** and **B** defects can be seen in Figs. 2(a) and 2(b). Also, sub-surface **A** defects can be seen with lighter contrast as previously reported[11] (see Fig. S1a in SI). Interestingly, we find that the nature of type-**B** defects, but not type-**A** defects, can be modified by an electrical pulse, applied with an STM tip (see Fig. S2 in SI). After the electrical pulse, defect-**B** now appears dumbbell shaped with a bright center (at negative bias), and a circular dark region with a relatively bright dot in the center (at positive bias), shown in Figs. 2(c-f). This suggests defect-**B** has switched to another type of defect, which we label as defect-**B′**. However, we see that defect-**A** remains a dumbbell at negative bias after application of the STM pulse. We note that this finding is in marked contrast to a very recent report in the literature,[17]

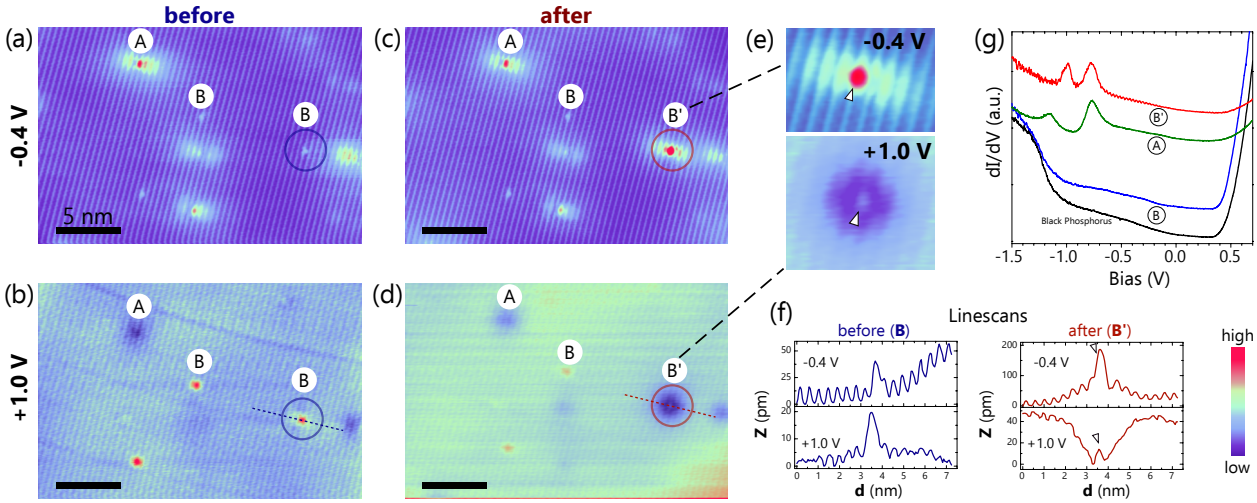

Figure 2: **Types of defects and switching by electrical pulse.** STM images of BP surface showing different types of defects at (a) negative (sample bias voltage $V = -400$ mV, current setpoint $I_t = 100$ pA), and (b) positive ($V = 1$ V, $I_t = 100$ pA) bias. Two main types of defects are identified based on their appearance and labeled as **A** and **B**. After local application of an electrical pulse, a defect-**B** defect (shown within blue circle) switches to defect-**B′** (shown within red circle); (c) negative and (d) positive bias STM images of the same area, after application of the electrical pulse. (e) Enlarged view of defect-**B′**. White triangular marker shows central bright spot at both polarities. (f) Line scan comparison of defects **B** and **B′** taken along armchair direction. The triangular marker identifies the presence of a relatively bright center in the dark region of defect-**B′** at positive bias [shown in (e)]. (g) STS spectra measured on defects **A**, **B** and **B′** and on the BP surface far from defects. The curves are offset for clarity.

where the authors found that their dumbbell-shaped features (identified as neutral MVs) changed to bright dots (identified as negatively charged MVs) upon application of a pulse.

While defects **A** and **B′** appear similar, there are subtle but important differences between them, apparent upon comparing either the STM images of Figs. 2(c) and 2(d) or the topography line scans in Fig. S3 of the SI. In negative bias, the relative contrast is higher for defect-**B′** than for defect-**A** near the center of the feature. Similarly, at positive bias, defect-**B′** (but not defect-**A**) has a bright dot in the center of the surrounding darker contrast region [see the marker in Fig. 2(e) and in the right panel of Fig. 2(f)].

Differences between defects **A**, **B** and **B′** also appear clearly in dI/dV spectra [Fig. 2(g)]. Previous studies have reported spectroscopic signatures of dumbbell defects, but focused only on a low energy range (below 0.4 eV). Different low energy characteristics have been reported such as two resonant states around the Fermi level separated by 27 meV,[11] two acceptor states at -0.13 eV and -0.21 eV,[12] or a peak at 0.02 eV and a shoulder at 0.12 eV.[16] We do not observe such low energy features, however we find clear electronic states at higher energies, as described below.

STS on defect-**B** yields a spectrum that is very similar to that of the BP region away from defects. In contrast, STS on defects **A** and **B′** shows two resonances located deep within the valence band [Fig. 2(g)]. While the position of the first peak is almost the same (around -0.7 V) for both these defects, the second peak is located slightly deeper for defect-**A** (-1.1 V) than for defect-**B′** (-1.0 V). From these electronic spectra, one can conclude that defect-**B′** bears more similarity to defect-**A** than to defect-**B**, which is also clear from the STM images.

In order to identify the nature of these defects, we have carried out spin-polarized DFT calculations for various possible defect configurations, using the Quantum ESPRESSO package[18,19] (details in SI). We consider several types of possible defects: three types of monovacancies (5656-MV-1, 5656-MV-2 and 59-MV), a Stone-Wales (SW) defect, a divacancy (DV), an interstitial Sn atom (Sn-int), and a substitutional Sn defect in SL 1 (Sn-1) or SL 2 (Sn-2); see Fig. S4 of SI. Note that Sn is used in the synthesis procedure; its presence is con-

firmed by X-ray photoemission spectroscopy (Fig. S5 of SI). We note that though there have been previous DFT calculations on different types of BP defects,[11,12,20–31] only 5656-MV-1 and Sn-1 configurations have been previously considered as candidates to explain dumbbell features seen in STM experiments.[11,12,16,17]

Our identification approach involves correlating the salient features in the experimental STM images of a given defect type with those in simulated images[32] of candidate defects at both bias polarities, for a precise identification. As an example, Fig. 3(a) contains a table listing 5 characteristic features of the experimental image of defect-**A**; see also markers in Figs. 1(e)-1(f). One can see that only for the simulated image of the Sn-2 defect are all five features matched, as illustrated in Figs. 3(b)-(g). We therefore conclude that defect-**A** corresponds to Sn-2. Our DFT calculations indicate that this defect is non-magnetic.

Previous authors[11] had attributed dumbbell features as arising from a MV, based on the fact that the charge density (obtained from tight-binding calculations) of a mid-gap state, resembles an asymmetric dumbbell in the neighborhood of such a monovacancy. Though we too find that the band-resolved electronic charge density, from DFT, for certain states around the monovacancy has a dumbbell shape (see Fig. S6 in the SI), the simulated STM image of the MV is not dumbbell-shaped [see Fig. S6(c)]. Moreover, in the simulated STM images at negative bias, all three monovacancies manifest as a dark feature, rather than the bright dumbbell seen in the experimental images of defect-**A**. At positive bias, we find that the MV is imaged as a dark circular spot [see Fig. S6 in the SI, and the table in Fig. 3(a)].

In order to gain greater insight into the origins of the shapes and contrasts of features seen in STM images, we introduce two new 'States Projected Onto Individual Layers' (SPOIL) quantities Δ_i and $D_{i,j}$, defined as follows:

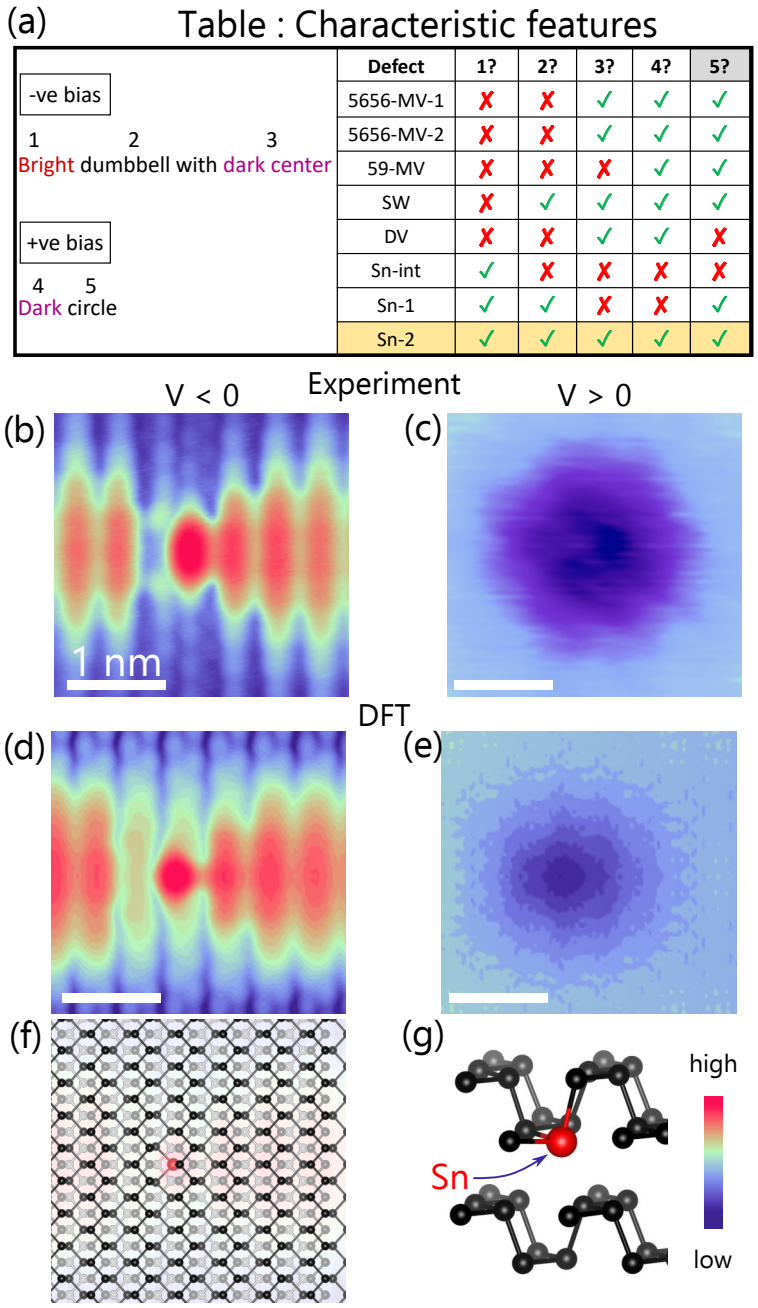

Figure 3: **Identification of defect-A: DFT and experiment** (a) Table identifying 5 features characteristic of STM images of defect-**A**. Of the 8 types of defects considered theoretically, only the Sn-2 defect is able to correctly reproduce all 5 features. Atomically resolved experimental STM image of defect-**A** at (b) negative bias ($V = -22$ mV, $I_t = 200$ pA), (c) positive bias ($V = +1$ V, $I_t = 100$ pA). Calculated STM images of the Sn-2 defect (isosurface $= 10^{-8}$ e/Bohr^3) at (d) -0.1 V and (e) $+0.91$ V. Relaxed geometry obtained from DFT of Sn-2. as seen from (f) top view and (g) side perspective view. For ease of understanding, there is also a faint background of the STM image of (d) in (f).

$$\Delta_i = \int_{\epsilon_F}^{\epsilon_F+eV} \pi_i(\epsilon) d\epsilon, \tag{1}$$

$$D_{i,j} = \int_{\epsilon_F}^{\epsilon_F+eV} P_{i,j}(\epsilon) d\epsilon, \tag{2}$$

where ϵ_F is the Fermi energy, e is the charge of the electron, V is the STM bias potential, and $\pi_i = \sum_j P_{i,j}(\epsilon)$, where $P_{i,j}(\epsilon) = \sum_n \langle\psi_n|\phi_i^j\rangle\langle\phi_i^j|\psi_n\rangle\delta(\epsilon - \epsilon_n)$.

Here, i is an atomic index, and $P_{i,j}(\epsilon)$ represents the density of states projected on the j^{th} orbital of the i^{th} atom. π_i is the total PDOS summed over all the orbitals for the i^{th} atom. ψ_n is the n^{th} Kohn-Sham orbital and ϕ_i^j is the j^{th} atomic orbital of the i^{th} atom. Δ_i gives the contribution of the i^{th} atom, and $D_{i,j}$ the contribution of the j^{th} orbital in the i^{th} atom, to the STM image at bias voltage V. The SPOIL quantities can accurately predict the shape of large-scale features seen in STM images, and phenomena such as a change of contrast upon changing bias voltage. However, compared to simulated STM images obtained using the Tersoff-Hamann approach,[32] they have the advantage that they allow easy interpretation about which orbitals are responsible for features observed in STM images; one can also gain information theoretically about how features such as defects perturb the electronic structure of interior layers.

In Figs. 4(a) and 4(e), we have plotted Δ_i for atoms in the topmost layer of the Sn-2 system. We see that at negative bias we get a bright dumbbell, and at positive bias a dark circular spot, as in the experimental STM images of defect-**A**. From the orbital contributions $D_{i,j}$ plotted in Figs. 4(b)–(d) and Figs. 4(f)–(h), we see that the p_z orbitals (which the STM tip can be expected to be particularly sensitive to) show clear evidence of the bright dumbbell/dark spot at negative/positive bias.

Following a similar procedure, we identify defect-**B** as an interstitial Sn atom between the first and second phosphorene layers [see Fig. 5(a)]. It is important to note that DFT finds this defect configuration also to be non-magnetic, i.e., it exhibits no spin polarization of the

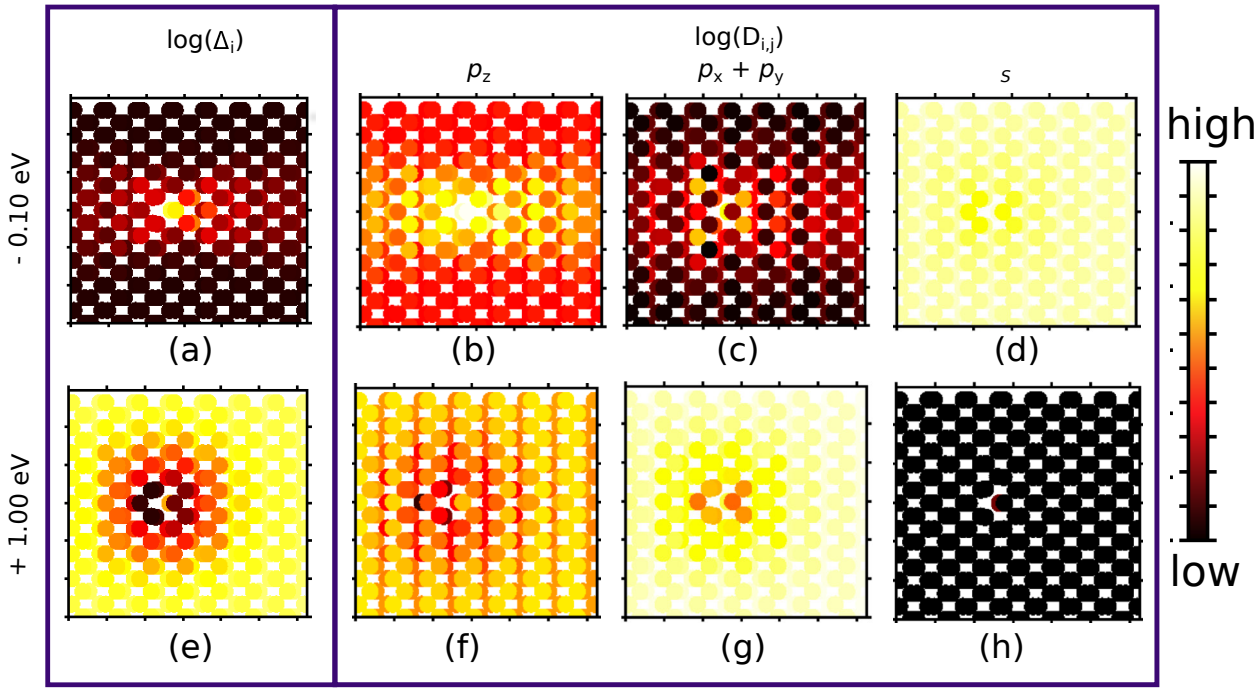

Figure 4: SPOIL quantities plotted for the topmost layer of atoms in the Sn-2 system (with a substitutional Sn impurity in the second phosphorene sub-layer). It is useful to compare these with experimental STM images of defect-**A**. In (a) and (e), all atoms are colored according to their value of Δ_i using a logarithmic scale; in the remaining panels they are colored according to their values of $D_{i,j}$. $j = p_z$ for (b) and (f), $j = p_x + p_y$ for (c) and (g), and $j = s$ for (d) and (h). The top panel is computed for bias voltage $V = -0.1$ V, and the bottom panel is computed for $V = +1.0$ V.

charge density. In Fig. S7 in the SI, we show SPOIL plots for these configurations; again, the p_z orbitals of atoms in the topmost phosphorene layer are responsible for the bright spot imaged at both negative and positive bias.

Next, we consider three most probable candidates for defect-**B′**: we call these Sn-2+P(gas phase), Sn-2+P-interstitial, and Sn-2+P-adatom [see Figs. 5(b)–(d)]. In all these configurations, the interstitial Sn atom in defect-**B** has now moved to a substitutional site in SL 2 of the top phosphorene layer. However, the configurations differ in where the P atom that has been substituted by the Sn atom has moved to: it is in the gas phase, or in an interstitial position, or an adatom, respectively. From DFT calculations, we find that all three configurations lie lower in energy than the starting configuration of defect-**B**: by 2.13 eV, 4.01 eV and 4.27 eV, respectively. Thus, the thermodynamically most favored configuration is for the Sn atom to be in the substitutional site in SL 2, and for the P atom to sit on the BP surface as an adatom. We therefore identify this configuration as corresponding to defect-**B′**. This identification is further supported by Sn-2+P-adatom leading to the simulated STM image which best matches experiment [Figs. 5(f)–(h), (j)–(l)]. A side by side comparison of simulated and experimental images is shown in Fig. S8. The defect formation energies for all three types of defects, viz., A, B and B' are given in the SI.

While we are confident that we have correctly identified the defect features imaged in our experiments, the question arises whether our results can also be used to interpret observations by other groups.[11,12,16,17] Differences in tunneling spectra, as well as varying behavior upon the application of an electrical pulse,[17] hint that the features observed by different groups may have different origins, possibly reflecting varying synthesis routes.[13]

From spin-polarized DFT calculations, we find that the configuration that we have identified as defect-**B′** (Sn-2+P-adatom) possesses a magnetic moment of 0.65 μ_B per defect. In Figs. 5(m) and 5(n), we show DFT results for the spin-polarized charge density in the vicinity of defect-**B′**. We see clear evidence of magnetism, spread over several Ångstroms. Thus, DFT suggests that by manipulation with the STM tip, we have not only changed the

positions of the P and Sn atoms, but we have also switched the system from a non-magnetic configuration to a magnetic one.

Finally, using our DFT results, we have computed the projected density of states (PDOS) for an atom in the vicinity of the defects [Fig. 5(o)]. Our calculations reproduce well the main features observed in STS on the different defects [compare Fig. 5(o) with Fig. 2(g)]. For **A** and **B′**, resonant states appear below the Fermi level, while defect-**B** shows a PDOS close to that of pristine BP. This agreement further supports the identification of the point defects that we observed experimentally.

In conclusion, we have investigated the origins of native defects in black phosphorus, including the ubiquitous dumbbell shaped defects, through DFT calculations combined with low temperature STM/STS experiments. We find an almost exact match between experimental STM images of these dumbbell defects with simulated STM images of Sn-2, a Sn impurity in the lower plane of the topmost phosphorene layer. This identification is further supported by the similarity between the computed PDOS plot for Sn-2 and the tunneling spectrum measured at the dumbbell center. Similarly, we have been able to identify a less stable defect, which appears as a dot in STM and rather featureless in STS, as an interstitial Sn atom. Upon the application of a voltage pulse, this defect transforms to another configuration, where the Sn atom replaces a nearby P atom. This identification is explained using calculated defect formation energies, PDOS plots and simulated STM images at both bias polarities. DFT calculations show that in this process, one switches from a non-magnetic to magnetic system, resulting from an adsorbed P-adatom atop Sn. We have also introduced SPOIL quantities which give atom-wise and orbital-wise contributions to features observed in STM images.

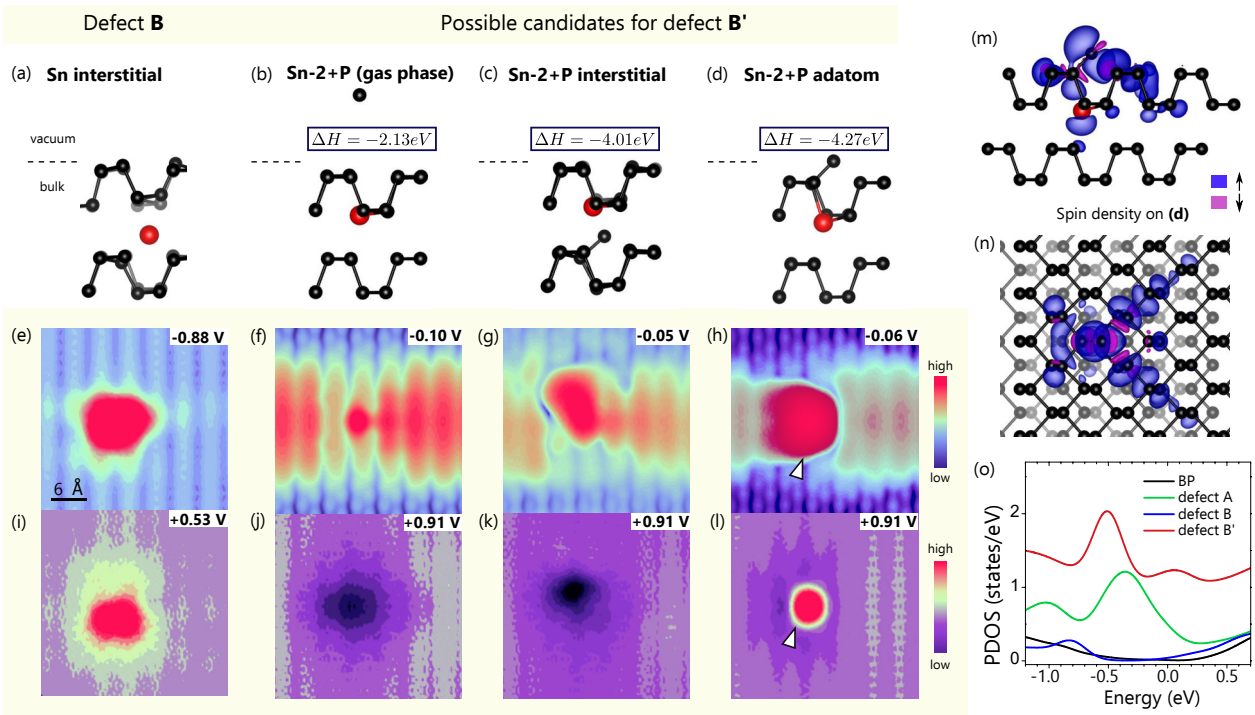

Figure 5: **Identification of defects B and B′.** Defect **B** is identified as the Sn-int configuration, whose structure is shown in (a), and simulated STM images in (e) and (i). Three possible structural re-arrangements after application of an electrical pulse, along with the computed changes in total energy, are shown in (b), (c) and (d). Corresponding simulated STM images are shown at (f), (g), (h) negative bias and (j), (k), (l) positive bias. Isosurface vlaues: (e,i) 5×10^{-9} e/Bohr^3, (f,j) 10^{-8} e/Bohr^3, (g,k) 10^{-8} e/Bohr^3, (h,l) 10^{-9} e/Bohr^3. Black and red spheres indicate P and Sn atoms, respectively, and all STM images are of size 3.1 nm $\times$ 3 nm. Panels (m) and (n) show side and top views of defect **B′**, along with isosurfaces of the spin polarized charge density (up spin − down spin; isosurfaces = ± 0.0003 e/Bohr^3) showing clearly that the system possesses a magnetic moment. (o) Calculated projected density of states (PDOS) for the defect configurations: Sn-2 (defect-**A**), Sn-int (defect-**B**) and Sn-2 + P-adatom (defect-**B′**) compared with that of pristine black phosphorus (BP). Fermi level at 0 eV.

Acknowledgement

We acknowledge the Indo-French Centre for the Promotion of Advanced Scientific Research (CEFIPRA) for funding our collaboration. We are especially grateful for assistance provided by the Late Ms. A. Sathidevi. We are grateful to the ANR and MOST (DEFINE2D project no. ANR-20-CE09-0023, MOST 110-2923-M-002 -010) for financial support, and the TUE-CMS, JNCASR and the Sheikh Saqr Laboratory, JNCASR, for computational resources. DS acknowledges support from the NPDF of the Science and Engineering Research Board (SERB), Government of India.

Supporting Information Available

Experimental and computational methods, STM and STS of pristine black phosphorus, switching of type-**B** defect, comparison of defect-**A** and defect-**B′**, structures of different types of defects considered, XPS data, DFT results on 5656-MV-1, SPOIL plots for Sn-int, Experimental and calculated STM images of defects **B** and **B′** and defect formation energies of defect-**A**, **B** and **B′**.

References

(1) Bridgman, P. Two new modifications of phosphorus. *J. Am. Chem. Soc.* **1914**, *36*, 1344–1363.

(2) Novoselov, K. S.; Geim, A. K.; Morozov, S. V.; Jiang, D.; Zhang, Y.; Dubonos, S. V.; Grigorieva, I. V.; Firsov, A. A. Electric field effect in atomically thin carbon films. *Science* **2004**, *306*, 666–669, Publisher: American Association for the Advancement of Science.

(3) Cai, Y.; Zhang, G.; Zhang, Y.-W. Layer-dependent band alignment and work function of few-layer phosphorene. *Sci. Rep.* **2014**, *4*, 6677.

(4) Tran, V.; Soklaski, R.; Liang, Y.; Yang, L. Layer-controlled band gap and anisotropic excitons in few-layer black phosphorus. *Phys. Rev. B* **2014**, *89*, 235319.

(5) Carvalho, A.; Wang, M.; Zhu, X.; Rodin, A. S.; Su, H.; Castro Neto, A. H. Phosphorene: from theory to applications. *Nat. Rev. Mater.* **2016**, *1*, 16061.

(6) Xia, F.; Wang, H.; Jia, Y. Rediscovering black phosphorus as an anisotropic layered material for optoelectronics and electronics. *Nat. commun.* **2014**, *5*, 4458.

(7) Luo, Z.; Maassen, J.; Deng, Y.; Du, Y.; Garrelts, R. P.; Lundstrom, M. S.; Ye, P. D.; Xu, X. Anisotropic in-plane thermal conductivity observed in few-layer black phosphorus. *Nat. Commun.* **2015**, *6*, 8572.

(8) Wang, X.; Jones, A. M.; Seyler, K. L.; Tran, V.; Jia, Y.; Zhao, H.; Wang, H.; Yang, L.; Xu, X.; Xia, F. Highly anisotropic and robust excitons in monolayer black phosphorus. *Nat. Nanotechnol.* **2015**, *10*, 517–521.

(9) Khatibi, A.; Petruzzella, M.; Shokri, B.; Curto, A. G. Defect engineering in few-layer black phosphorus for tunable and photostable infrared emission. *Opt. Mater. Express* **2020**, *10*, 1488–1496.

(10) Zhang, C. D.; Lian, J. C.; Yi, W.; Jiang, Y. H.; Liu, L. W.; Hu, H.; Xiao, W. D.; Du, S. X.; Sun, L. L.; Gao, H. J. Surface structures of black phosphorus investigated with scanning tunneling microscopy. *J. Phys. Chem. C* **2009**, *113*, 18823–18826.

(11) Kiraly, B.; Hauptmann, N.; Rudenko, A. N.; Katsnelson, M. I.; Khajetoorians, A. A. Probing single vacancies in black phosphorus at the atomic level. *Nano lett.* **2017**, *17*, 3607–3612.

(12) Qiu, Z.; Fang, H.; Carvalho, A.; Rodin, A.; Liu, Y.; Tan, S. J.; Telychko, M.; Lv, P.; Su, J.; Wang, Y. et al. Resolving the spatial structures of bound hole states in black phosphorus. *Nano lett.* **2017**, *17*, 6935–6940.

(13) Riffle, J.; Flynn, C.; St. Laurent, B.; Ayotte, C.; Caputo, C.; Hollen, S. Impact of vacancies on electronic properties of black phosphorus probed by STM. *J. Appl. Phys.* **2018**, *123*, 044301.

(14) Tian, Z.; Gan, Y.; Zhang, T.; Wang, B.; Ji, H.; Feng, Y.; Xue, J. Isotropic charge screening of anisotropic black phosphorus revealed by potassium adatoms. *Phys. Rev. B* **2019**, *100*, 085440.

(15) Kiraly, B.; Knol, E. J.; Volckaert, K.; Biswas, D.; Rudenko, A. N.; Prishchenko, D. A.; Mazurenko, V. G.; Katsnelson, M. I.; Hofmann, P.; Wegner, D. et al. Anisotropic two-dimensional screening at the surface of black phosphorus. *Phys. Rev. Lett.* **2019**, *123*, 216403.

(16) Wentink, M.; Gaberle, J.; Aghajanian, M.; Mostofi, A. A.; Curson, N. J.; Lischner, J.; Schofield, S. R.; Shluger, A. L.; Kenyon, A. J. Substitutional tin acceptor states in black phosphorus. *J. Phys. Chem. C* **2021**, *125*, 22883–22889.

(17) Fang, H.; Gallardo, A.; Dulal, D.; Qiu, Z.; Su, J.; Telychko, M.; Mahalingam, H.; Lyu, P.; Han, Y.; Zheng, Y. et al. Electronic self-passivation of single vacancy in black phosphorus via ionization. *Phys. Rev. Lett.* **2022**, *128*, 176801.

(18) Giannozzi, P.; Baroni, S.; Bonini, N.; Calandra, M.; Car, R.; Cavazzoni, C.; Davide Ceresoli,; Chiarotti, G. L.; Cococcioni, M.; Dabo, I. et al. QUANTUM ESPRESSO: a modular and open-source software project for quantum simulations of materials. *J. Phys. Condens. Matter* **2009**, *21*, 395502.

(19) Giannozzi, P.; Andreussi, O.; Brumme, T.; Bunau, O.; Nardelli, M. B.; Calandra, M.; Car, R.; Cavazzoni, C.; Ceresoli, D.; Cococcioni, M. et al. Advanced capabilities for

materials modelling with Quantum ESPRESSO. *J. Phys. Condens. Matter* **2017**, *29*, 465901.

(20) Cai, Y.; Ke, Q.; Zhang, G.; Yakobson, B. I.; Zhang, Y.-W. Highly itinerant atomic vacancies in phosphorene. *J. Am. Chem. Soc.* **2016**, *138*, 10199–10206.

(21) Gaberle, J.; Shluger, A. L. Structure and properties of intrinsic and extrinsic defects in black phosphorus. *Nanoscale* **2018**, *10*, 19536–19546.

(22) Kundu, S.; Naik, M. H.; Jain, M. Native point defects in mono and bilayer phosphorene. *Phys. Rev. Materials* **2020**, *4*, 054004.

(23) Rijal, B.; Tan, A. M. Z.; Freysoldt, C.; Hennig, R. G. Charged vacancy defects in monolayer phosphorene. *Phys. Rev. Mater.* **2021**, *5*, 124004.

(24) Hu, T.; Dong, J. Geometric and electronic structures of mono- and di-vacancies in phosphorene. *Nanotechnology* **2015**, *26*, 065705.

(25) Srivastava, P.; Hembram, K. P. S. S.; Mizuseki, H.; Lee, K.-R.; Han, S. S.; Kim, S. Tuning the electronic and magnetic properties of phosphorene by vacancies and adatoms. *J. Phys. Chem. C* **2015**, *119*, 6530–6538.

(26) Li, X.-B.; Guo, P.; Cao, T.-F.; Liu, H.; Lau, W.-M.; Liu, L.-M. Structures, stabilities and electronic properties of defects in monolayer black phosphorus. *Sci. Rep.* **2015**, *5*, 10848.

(27) Hu, W.; Yang, J. Defects in phosphorene. *J. Phys. Chem. C* **2015**, *119*, 20474–20480.

(28) Umar Farooq, M.; Hashmi, A.; Hong, J. Anisotropic bias dependent transport property of defective phosphorene layer. *Sci. Rep.* **2015**, *5*, 12482.

(29) Guo, Y.; Robertson, J. Vacancy and doping states in monolayer and bulk black phosphorus. *Sci. Rep.* **2015**, *5*, 14165.

(30) Sun, X.; Wang, Z. Sodium adsorption and diffusion on monolayer black phosphorus with intrinsic defects. *Appl. Surf. Sci.* **2018**, *427*, 189–197.

(31) Rezaee, A. E.; Almasi Kashi, M.; Baktash, A. Stone-Wales like defects formation, stability and reactivity in black phosphorene. *Mater. Sci. Eng. B* **2018**, *236-237*, 208–216.

(32) Tersoff, J.; Hamann, D. R. Theory of the scanning tunneling microscope. *Phys. Rev. B 31*, 805.